Selective Activation of Propane Using Intermediates Generated During Water Oxidation

Haochen Zhang,† Chunsong Li,† Qi Lu,†* Mu-Jeng Cheng,‡* and William A. Goddard III§*

†State Key Laboratory of Chemical Engineering, Department of Chemical Engineering, Tsinghua University, Beijing 100084, China; ‡Department of Chemistry, National Cheng Kung University, Tainan 701, Taiwan; §Materials and Process Simulation Center, California Institute of Technology, Pasadena, California 91125, USA

ABSTRACT: Electrochemical conversion of light alkanes to high-value oxygenates provides an attractive avenue for eco-friendly utilization of these hydrocarbons. However, such conversion under ambient conditions remains exceptionally challenging due to the high energy barrier of C-H bond cleavage. Herein, we investigated theoretically the partial oxidation of propane on a series of single atom alloys using active intermediates generated during water oxidation as the oxidant. We show that by controlling the potential and pH, stable surface oxygen atoms can be maintained under water oxidation conditions. The free energy barrier for C-H bond cleavage by the surface oxygen can be as small as 0.54 eV, which can be surmounted easily at room temperature. Our calculations identified three promising surfaces as effective propane oxidation catalysts. Our complementary experiments demonstrated the partial oxidation of propane to acetone on Ni doped Au surfaces. We also investigated computationally the steps leading to acetone formation. These studies show that the concept of exploiting intermediates generated in water oxidation as oxidants provides a fruitful strategy for electrocatalyst design to efficiently convert hydrocarbons into value-added chemicals.

INTRODUCTION

Converting light alkanes such as methane, ethane and propane to high-value oxygenates (e.g., alcohols, acetaldehyde and ketones) enables better utilization and storage of these hydrocarbon resources. However, partially oxidizing these alkanes is particularly challenging due to the very high activation energy of C-H bond cleavage.[1-3] The reaction conditions that can initiate the conversion can also oxidize those desired oxygenates, leading to unwanted products, such as fully oxidized carbon dioxide. Electrochemical methods provide promising avenues to circumvent this impediment because the external driving force (i.e., potential) can be controlled precisely. Moreover, as an anodic reaction, electrochemical oxidation of alkanes can be coupled with cathodic reactions, such as CO_2 or water reduction to produce hydrocarbons or hydrogen simultaneously.[4-7] Electrochemical devices also enable on-site transformation of alkanes where centralized steam reforming infrastructures are inaccessible.[8] Previous research attempts include direct oxidation[9], oxidation using metal redox couples[10-12], and oxidation using free radicals generated in a coupled oxygen reduction reaction (ORR)[13]. However, due to the large reaction barrier for C-H bond activation and the lack of effective oxidants, elevated pressure or temperature is typically employed to achieve appreciable activities.

The highly reactive atomic surface oxygen (*O) has been found to promote C–H activation in many thermo-catalysis systems with gaseous oxygen.[14-19] The *O can also be electrochemically generated in-situ via water oxidation or ORR. Experimental results show that *O formed during ORR can be utilized to activate light alkanes to produce oxygenates.[20-24] However, the efficiency remains low for its facile reduction along the ORR pathway to H_2O due to the lack of a rationally designed catalyst surface and the unstable *O. In addition, mixing alkanes with O_2 may be undesirable for practical applications because of the potential for combustion or explosion. Thus, we propose that to achieve an improved C-H cleavage barrier it is more advantageous to design a novel catalyst surface that can stabilize *O along the route of water oxidation.

Single atom alloys (SAAs) provide a promising class of catalysts to exploit the *O generated during water oxidation for partial oxidation of light alkanes. SAAs are typically bimetallic alloys composed of small amounts of isolated, catalytically active metal atoms doped at the surface layer of a relatively inert metal host. Due to isolation of SAA active centers, the alkanes can only attach to a limited number of *O, preventing over oxidation. In addition, the bimetallic nature of SAAs allows for decoupling of reactant activation and intermediate adsorption, which can circumvent the limits of the known scaling relationships.[25-26]

However, experimental rapid screening of potential SAA catalysts is difficult. Different SAAs usually require different synthesis methods and their preparations can be extremely sophisticated.[26] In this regard, theoretical investigation can provide a powerful and convenient tool to investigate the nature of this catalytic reaction on a variety of SAAs with controllable compositions. Herein, we take propane as a probe molecule and use density functional theory (DFT) combined with a constant electrode potential model[27-30] to investigate alkane activation by *O generated through water oxidation on SAAs.

The model SAAs are constructed on gold and silver hosts due to their high standard reduction potential and common utilization in experimental synthesis.[31-34] We constructed the SAA surface by replacing a surface Au or Ag atom with a heteroatom (**M**) to achieve a surface concentration of 1/9 on a three-layered 3×3 (111) surface. We investigated face-centered cubic dopant metals: Mn, Fe, Ni, Ru, Pd, and Ir. We denote an SAA with a dopant **M** as **M**@Au or **M**@Ag depending on its host. Among all SAA surfaces examined, we identified three promising candidates with low free energy reaction barriers for propane activation under ambient conditions. Then, to validate these predictions we carried out experiments demonstrating that propane can be successfully converted to acetone on Ni@Au surface

prepared using underpotential deposition (UPD). The subsequent reaction pathway towards acetone formation was determined by DFT calculations.

RESULTS AND DISCUSSION

Surface Pourbaix Diagrams. Our study begins by analyzing the surface Pourbaix diagrams under water oxidation conditions to determine the formation of stable *O on SAAs. Water oxidation has been proposed to proceed via four steps:[35]

$$* + H_2O \rightarrow *OH + H^+ + e^- \quad (a)$$

$$*OH \rightarrow *O + H^+ + e^- \quad (b)$$

$$*O + H_2O \rightarrow *OOH + H^+ + e^- \quad (c)$$

$$*OOH \rightarrow * + O_2 + H^+ + e^- \quad (d)$$

The principle for constructing surface Pourbaix diagrams is that the surface will be dominated by the reactant of the *first energetically uphill* step along the water oxidation pathways.[36] To obtain reaction free energies at the potential and pH of interest, we first calculated the formation free energy of water oxidation intermediates (i.e., *OH, *O and *OOH) at five discrete potentials (0.00, 0.50, 1.00, 1.23 and 1.50 V vs standard hydrogen electrode, henceforth denoted as V_{SHE}) using a clean SAA surface and $H_2O(l)$ as the references. Typical structures of these intermediates are shown in Figure 1. On all SAAs except those based on Ir, we find that intermediates favor the 3-coordinate site composed of the dopant and two substrate atoms, while the site on top of the Ir atom is preferred for Ir-based SAAs. Then we calculated the reaction free energy of each step based on the formation free energy of these intermediates at those discrete potentials. By linear fitting the calculated values against potentials, we obtained equations describing reaction free energies as a function of potential. Then we added the -0.0592 eV × pH term to account for the influence of pH on the reaction free energy. The resulting equations were used to construct the surface Pourbaix diagram for each SAA surface (Table S1).

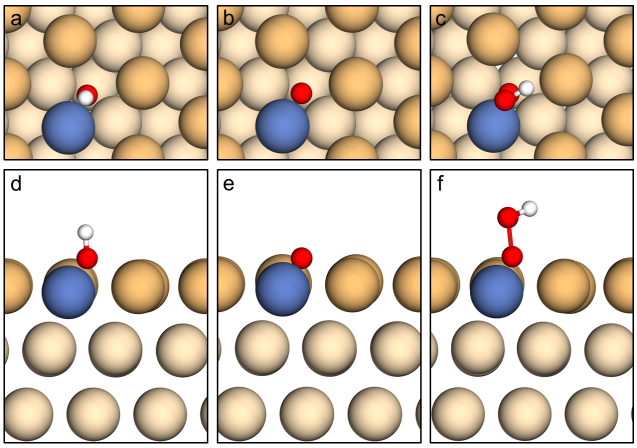

Figure 1. Top view (**a**, **b**, **c**) and side view (**d**, **e**, **f**) of water oxidation intermediates *OH (**a**, **d**), *O (**b**, **e**) and *OOH (**c**, **f**). Mustard and beige balls represent the top layer and bottom layer of substrate atoms, respectively. Blue, red and white balls stand for dopant, oxygen and hydrogen atoms, respectively.

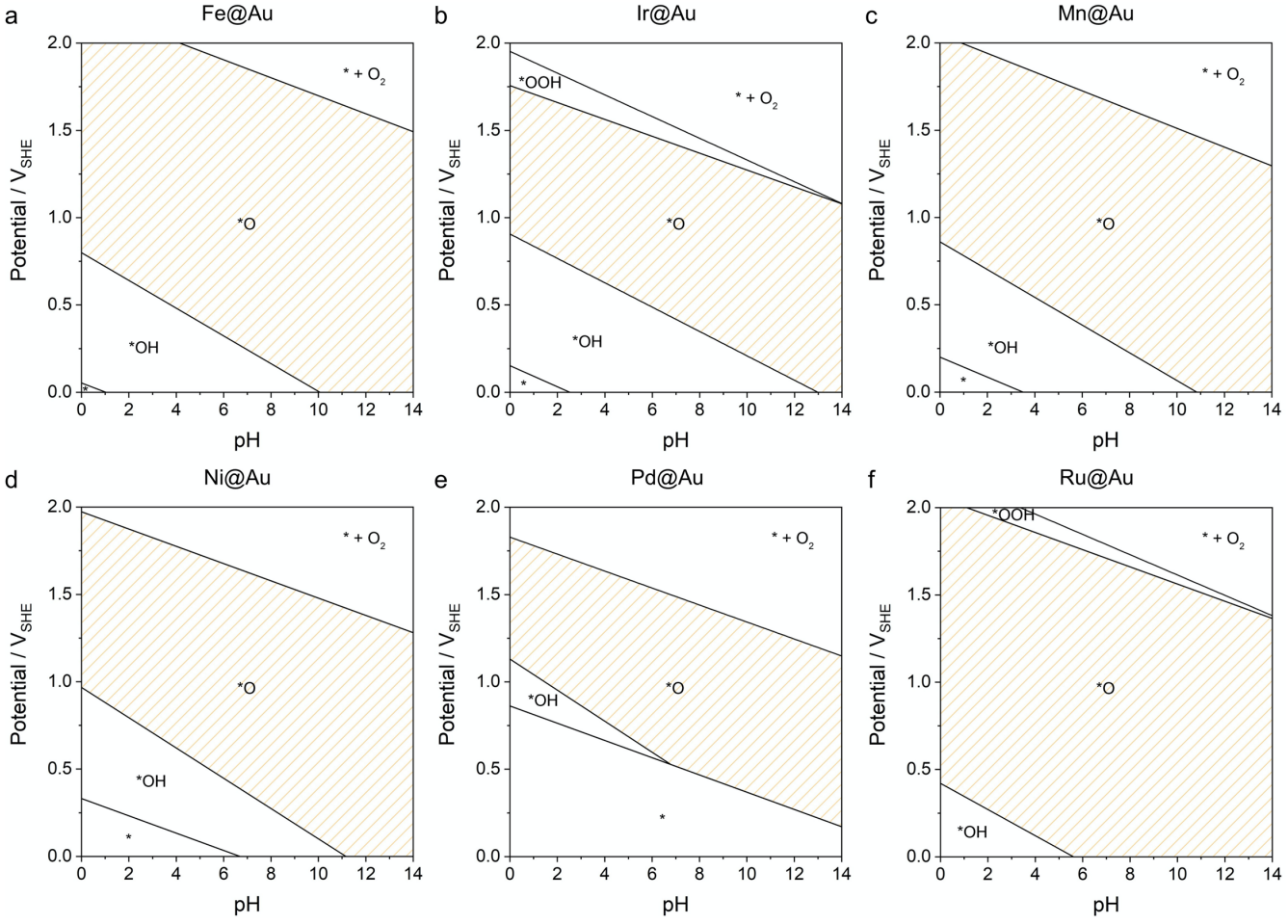

Figure 2. Surface Pourbaix diagram for Au-based SAAs constructed at 298K and 1 atm. Striped areas indicate the pH and potential range at which *O is present on the surface.

As shown in Figure 2 and Figure S1, the surface Pourbaix diagrams depend highly on the composition of SAA. Most importantly, *O is stable on all SAAs over a large range of potential and electrolyte pH, facilitating experimental manipulation. (up to 81% and 90% of the area in the Pourbaix diagrams for Au- and Ag-based SAAs, respectively). In comparison, pristine Au and Ag exhibit narrower windows to provide stable *O (i.e., 43% and 17% of the area for pristine Au and Ag, respectively, Figure S2), which is consistent with the literature showing that metal-oxo groups are not favorable on Au and Ag surfaces.[37-38] Thus, the increased affinity to oxygen of our **M**@Au and **M**@Ag surfaces is due to the higher oxophilicity of the dopant atoms.[39-40] At low potentials and pH, stable *O does not form on all SAAs. Some SAAs are covered by *OH (i.e., Fe@Ag, Ir@Ag, Mn@Ag, Ni@Ag, Ru@Ag, Ru@Au). Other SAAs will expose a clean surface (i.e., Pd@Ag, Fe@Au, Ir@Au, Mn@Au, Ni@Au, Pd@Au). At high potentials, oxygen is eventually produced on all SAA surfaces. Thus, our calculations show that by adjusting pH and potential, *O can be stabilized on the surface for propane C-H activation.

Propane Activation by *O. Since *O can exist on all SAAs, we calculated free energy barriers ($\Delta G_{CH}^{\ddagger}$) and reaction free energies (ΔG_{CH}) for propane activation by *O (Table 1 and Table S2). We examined cleavage of the secondary C-H bond (on the -CH_2- group) since this bond is ~ 3 kcal/mol weaker than on the primary carbon.[1-2] The reaction we examined involves C-H bond cleavage through hydrogen abstraction by *O to form an O-H bond plus a C-substrate bond (Figure 3). As in Table 1, the barriers for propane activation lie in the range of 0.57~1.32 eV for the potentials examined. Notably, Au-based SAAs exhibit smaller free energy barriers for C-H bond cleavage than Ag-based counterparts, which will be analyzed in detail in the following paragraphs. Importantly, at potentials higher than 0.50 V_{SHE}, Fe@Au, Ni@Au, and Pd@Au exhibit barriers smaller than 0.75 eV, a threshold required for fast kinetics.[41] These three SAAs are promising catalysts for propane activation using *O. In contrast, the other SAAs show large free energy barriers, indicating a sluggish reaction rate unsuitable for a practical catalyst.

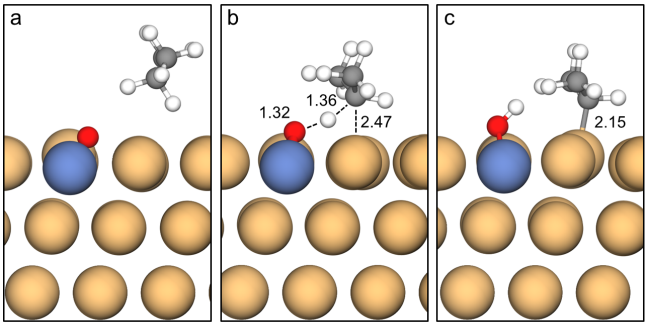

Figure 3. The initial state (**a**), transition state (**b**) and final state (**c**) of C-H bond cleavage on Ni@Au, as an illustration. Mustard, blue, red, grey and white balls stand for gold, nickel, oxygen, carbon and hydrogen atoms, respectively. Numbers (Å) are distances between atoms connected with a bond or a dash line.

As mentioned above, the activation of propane involves concomitant formation of an O-H bond and a C-substrate bond. Thus, it is reasonable to correlate the free energy barriers with both O-H bond formation free energy ($\Delta G_{O\text{-}H}$) and propyl adsorption free energy (ΔG_{Pr}). As shown in Eq. 1, we find a good linear correlation with a mean absolute error of 0.075 eV (See Table 1, Table S3 and Table S4 for detailed data). 77% of the data points locate within the range of ± 0.1 eV of the prediction from Eq. 1, within the typical accuracy for DFT PBE-D2 compared to experiments (Figure 4).[42-43] This small error is sufficient to make a rough estimate of the free energy barriers for propane activation. Our correlation suggests that a higher affinity of alkyl groups for the surface and a stronger O-H bond will facilitate C-H bond cleavage in alkane activation. Moreover, the affinity of alkyl groups plays a more important role in determining the barrier than O-H bond strength because the weight of ΔG_{Pr} (0.44) in the correlation is greater than that of $\Delta G_{O\text{-}H}$ (0.35). In addition, this correlation (Eq. 1) can be used to predict free energy barriers of C-H bond cleavage using $\Delta G_{O\text{-}H}$ and ΔG_{Pr} which are easily obtained with much less computational resources.

Table 1. Free energy barriers (eV) for C-H bond cleavage by *O under several potentials

SAAs	0.00 V_{SHE}	0.50 V_{SHE}	1.00 V_{SHE}	1.23 V_{SHE}	1.50 V_{SHE}
Fe@Au	0.93	0.81	0.71	0.67	0.64
Ir@Au	0.93	0.81	0.70	0.97	0.93
Mn@Au	1.04	0.94	0.84	0.78	0.76
Ni@Au	0.89	0.78	0.69	0.62	0.57
Pd@Au	0.91	0.81	0.73	0.70	0.68
Ru@Au	1.24	1.10	0.93	1.04	0.97
Fe@Ag	1.18	1.10	1.04	1.05	1.12
Ir@Ag	1.17	1.32	1.00	0.95	1.23
Mn@Ag	1.23	1.14	1.04	1.12	1.28
Ni@Ag	1.10	0.99	0.95	0.88	0.88
Pd@Ag	0.91	0.88	0.88	0.84	1.01
Ru@Ag	1.16	1.08	1.13	1.27	1.29

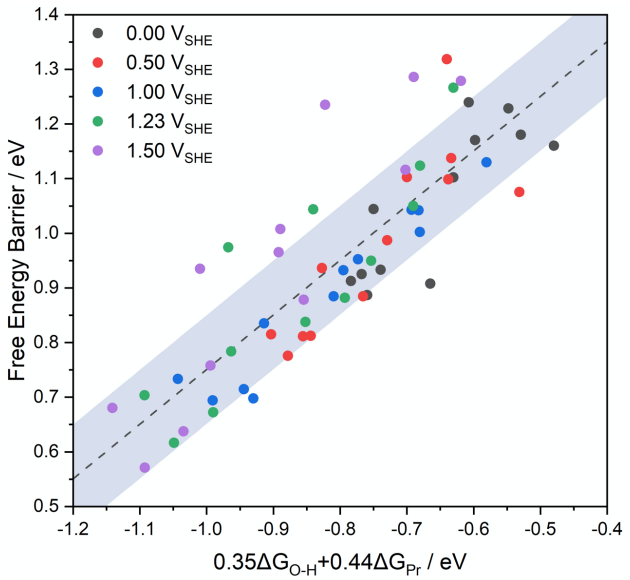

Figure 4. Linear correlation between free energy barriers and a combination of O-H bond formation free energy ($\Delta G_{O\text{-}H}$) and propyl adsorption free energy (ΔG_{Pr}). The shaded area is the range predicted by Eq. 1 ± 0.1 eV.

$$\Delta G_{CH}^{\ddagger} = 0.35\Delta G_{O\text{-}H} + 0.44\Delta G_{Pr} + 1.75 \text{ eV} \quad (1)$$

Similar correlations were reported in methane activation by Tsai et al.[44] In their work, the free energy barrier of methane activation was correlated linearly to the sum of the adsorption free energy of methyl group and the bond formation free energy between hydrogen and a surface promoter. We note that Latimer et al. reported that the energy barrier of C-H bond activation is determined only by the hydrogen affinity of the catalyst.[45] This is because the final state of the activation process in their system is radical-like, in which no chemical bond was formed to the catalyst surface.

By analyzing the ΔG_{Pr} and $\Delta G_{O\text{-}H}$ of all SAAs, we find that the mean absolute difference (MAD) between ΔG_{Pr} on Au- and Ag-based surfaces is 0.59 eV, which is significantly larger than the corresponding MAD between $\Delta G_{O\text{-}H}$ (i.e., 0.11 eV) (Table S3 and S4). This indicates that the higher affinity of the alkyl group may be the main reason that barriers for C-H cleavage on Au-based SAAs are generally smaller than that on Ag-based counterparts. In our system, the C-H activation proceeds via a surface-assisted pathway, which is supported by a relatively short C-substrate distance (2.426 ~ 2.531 Å, see Table S5 for detailed data) in the transition state compared to that under non-interactive conditions (> 3 Å). The higher affinity of the propyl group will stabilize the transition state (Figure 3) to obtain a lower the reaction free energy barrier.

Electrochemical Oxidation of Propane. Based on our computational results, we conducted propane electrolysis experiments on Ni@Au as a proof-of-concept. The Ni@Au was chosen because it has the lowest predicted free energy barrier for propane activation (Table 1). To construct the model catalyst, a monolayer of Ni was firstly deposited via UPD on Au foil and subsequently stripped by anodic dissolution according to an established method (Figure S3).[46] We expect that at low concentration Ni atoms are dispersed on Au surface because it is unlikely to remove all Ni atoms by electrochemical leaching, as suggested by many previous studies.[32, 47-52] The electrolyte was 0.1 M H_2SO_4 (pH = 0.7). Acetone was identified as the major liquid-phase product at 1.80 V_{SHE} on Ni@Au based on nuclear magnetic resonance (NMR) spectroscopy (Figure 5 and Figure S4). The concentration of acetone produced is 10.4 µmol/L after 12-h electrolysis. Trace amounts of iso-propanol were also detected. The gas-phase products were below detection limit of our gas chromatography. The production of acetone on Ni@Au increases with electrolysis time (Figure 5a and b). In control experiments on pristine Au foil at 1.80 V_{SHE}, the concentration of acetone produced after 12-h electrolysis was only 0.014 µmol/L, suggesting that Ni@Au, not pristine Au, is the catalyst surface for acetone production (Figure S4). Under Ar atmosphere, no product was detected on Ni@Au under otherwise identical conditions, confirming that acetone is produced from propane electrolysis (Figure S4).

Electrolysis at 1.70 V_{SHE} shows similar trends of acetone production as 1.80 V_{SHE} with lower rates (Figure 5a). The production of acetone becomes undetectable at further reduced applied potential. These applied potentials are slightly higher than the computationally predicted values, most likely due to the known error of DFT calculations compared to experiment.[42-43] However, the predicted trend that C-H cleavage barrier decreases at increasing potential is consistent with experimental results that acetone production rate increases at larger applied potential.

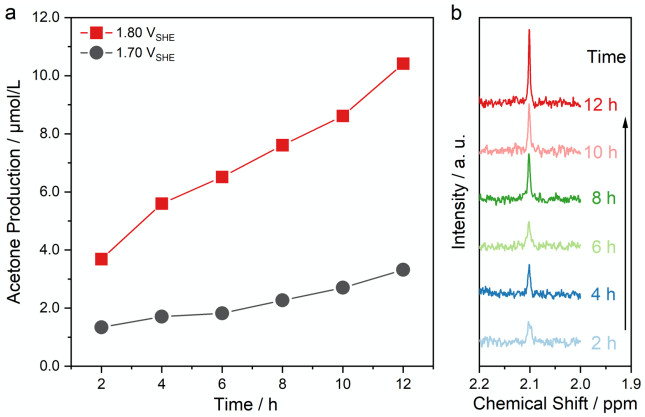

Figure 5. (**a**) Time-dependent acetone production on Ni@Au in 12-hour propane electrolysis experiments at different potentials. (**b**) NMR spectra of electrolytes on Ni@Au at different electrolysis time. All spectra are scaled such that the areas of the internal standard are the same.

Reaction Pathway towards Propane. Based on experimental identification, acetone is considered as the main product of propane conversion on Ni@Au. We then used DFT calculations to investigate the subsequent steps after C-H bond activation leading to acetone formation on Ni@Au at 1.80 V_{SHE} and pH of 0.7. The free energy diagram towards acetone was also investigated on pristine Au as a comparison. Both kinetics and thermodynamics were considered. The results in Figure 6 show that all steps towards acetone on Ni@Au are thermodynamically downhill. The rate-determining step along the pathway for acetone formation is cleavage of the secondary C-H of propane, leading to the highest free energy barrier of 0.54 eV (TS1 in Figure 6). This C-H cleavage of propane leads to formation of *OH and *$CH(CH_3)_2$ (*Pr). A proton-electron pair is expected to be removed easily from *OH to generate *O because of the very oxidative condition. Then the generated *O recombines with the *$CH(CH_3)_2$, leading to the formation of *$OCH(CH_3)_2$ (*OPr) with $\Delta G^{\ddagger}/\Delta G$ = 0.25/-0.85 eV (TS2 in Figure 6). One more proton-electron pair is quickly removed from *$OCH(CH_3)_2$, resulting in acetone formation with ΔG = -2.76 eV. In contrast, the C-H cleavage on pristine Au is prohibited kinetically due to a much higher free energy barrier of 1.29 eV, indicating that only Ni@Au sites are responsible for the oxidation of propane.

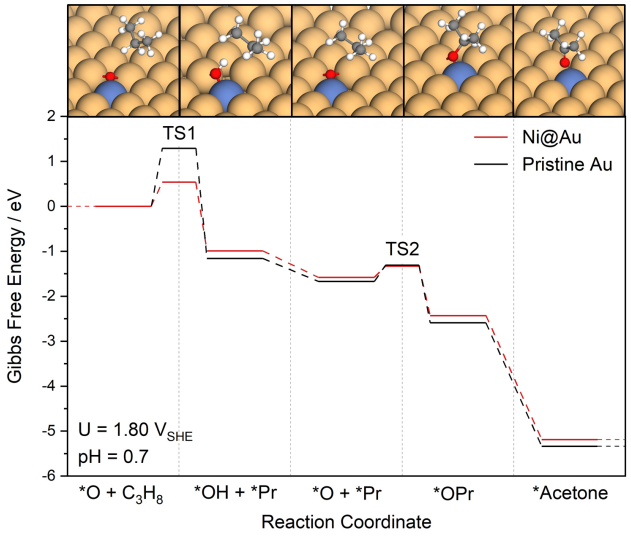

Figure 6. The free energy diagram for propane oxidation to acetone on Ni@Au (red) and pristine Au (black). Structures for each reaction step on Ni@Au are provided on top. Mustard, blue, red, grey and white balls stand for gold, nickel, oxygen, carbon and hydrogen atoms, respectively.

We note that *OH could be a potential oxidant and may play a role as a side reaction in propane oxidation. However, we consider that *OH is unlikely to exist on the electrode surface at a positive potential of 1.8 V_{SHE} as indicated by the surface Pourbaix diagrams (Figure 2).

CONCLUSIONS

In this study, we investigated the partial electro-oxidation of propane to oxygenates using *O generated during water oxidation. We screened surface Pourbaix diagrams for 12 SAAs to find that *O is stable over a considerable range of potential and pH. We then calculated free energy barriers of propane C-H bond cleavage using *O as the oxidant to identify Fe@Au, Ni@Au, and Pd@Au as promising catalysts. We validated our predictions with complementary electrolysis of experiments with propane on Ni@Au prepared via UPD of Ni on Au foil. We achieved acetone concentrations as high as 10.4 μmol/L after 12-hour electrolysis on Ni@Au. Our DFT calculations identified the reaction sequence in acetone production as *O + $CH_2(CH_3)_2$ → *OH + *$CH(CH_3)_2$ → *O + *$CH(CH_3)_2$ → *$OCH(CH_3)_2$ → *$OCH(CH_3)_2$. The rate-determining step for acetone formation is the initial propane C-H cleavage with a free energy barrier of 0.54 eV at a potential of 1.80 V_{SHE} and pH = 0.7.

Our investigation shows that *O generated during water oxidation can be an effective oxidant for light alkane activation, providing new insights in the design of efficient electrocatalysts for better utilizations of these hydrocarbon.

EXPERIMENTAL SECTION

Computational details. To simulate the surface of pristine Au or Ag, we used an Au(111) or Ag(111) metal slab (3 × 3) consisting of 3 layers with the bottom layer fixed in its bulk position. One atom of the top layer was replaced with a heteroatom to simulate the SAA with a surface concentration of 1/9. The total energy of the slab with different adsorbates was calculated using the projector augmented wave (PAW) method as implemented in the spin-polarized Vienna ab initio Simulation Package (VASP).[53-56] The exchange–correlation interaction was treated with the Perdew-Burke-Ernzerhof functional.[57] The plane-wave cut off was set to 400 eV. The semi-empirical D2 approach as implemented in VASP was employed to describe the van der Waals (vdW) interactions.[58] Because the vdW parameters for Au were not provided in the original paper, we adopted 40.62 J·nm^6/mol for the dispersion coefficient (C_6) and 1.772 Å for the vdW radius (R_0).[59] These values were used by Amft et al.[54] in their study of adsorption of Au atoms on graphene. All calculated energy values were extrapolated to k_BT= 0. A Monkhorst–Pack k-point net of 4 × 4 × 1 was chosen to sample the reciprocal space. A vacuum of 50 Å was introduced to each side to avoid interactions between successive metal slabs.

To establish the electrochemical interface, we applied the approach proposed by Head-Gordon et al. and Goddard et al.[27-30] In this model, the Fermi energy is adjusted to a target value by changing the number of electrons in the system during each step of the geometry optimization, which keeps the work function and electrode potential constant in the calculations. Then the linear Poisson–Boltzmann implicit solvation model with a Debye screening length of 3.0 Å was used to neutralize the non-zero charge in the simulation cell and to simulate water and the electrolyte, allowing for a more realistic description of the electrochemical double layer. The free energy of H^+/e^- pair was estimated on the basis of the computational hydrogen electrode model, which states that, $G_{H^+/e^-} = 0.5G_{H_2(g)}$ - eU - 0.0592 eV × pH.[60] A detailed description of this approach has been provided in our previous works.[61-62]

The transition state for each reaction was first approached using the nudged elastic band (NEB) method for the neutral state.[63] Forces on the climbing image were converged to <0.02 eV $Å^{-1}$. The plane-wave cutoff, smearing parameter, functional, and calculator parameters were the same as those used in slab geometry optimizations. Structures obtained from NEB were employed to generate the input structure and orientation for the dimer calculation.[64] The force of the dimer calculation was converged to <0.1 eV $Å^{-1}$ to accurately locate the saddle point, i.e., the transition state. The transition states were verified with vibrational frequency analysis. After that, the single point transition state energy was calculated for constant potential. We performed several test calculations to compare the single point energies with the energies after structural optimization and found that the differences are less than 0.01 eV (Table S6). Therefore, the single point energy under potentials were used to represent the energy of transition state to save computational resources.

Electrochemical oxidation of propane. Gold foil (thickness 0.127 mm, 99.99%) and Ni foil (thickness 0.1 mm, 99.994%) were purchased from Alfa Aesar. Nickel (II) sulfate (99.99%), sulfamic acid (99.5%) and sulfuric acid (ACS reagent, 95.0 ~ 98.0%) were purchased from Sigma-Aldrich. Propane (99.99%) and argon (99.999%) was purchased from Air Liquide. Gold foil was annealed at 300°C in ambient atmosphere for 3h, etched in fresh aqua regia for 30s and then rinsed in deionized water (18.2 MΩ cm, Milli-Q) thoroughly prior to experiments. Ni foil was polished mechanically using sand paper (1200G, 3M) and cleaned in ultrasonic bath with deionized water prior to experiment.

UPD of Ni on Au was conducted in a one-compartment electrochemical cell according to a previous report.[46] A clean Au foil and a AgCl/Ag electrode (3.0 M NaCl, BASi®) was used as the working and reference electrode, respectively. A reticulated vitreous carbon electrode (BASi®) was used as a counter electrode to minimize the difference of electric field on Au foil. A solution containing 0.1M H_2SO_4, 0.1 M sulfamic acid and 0.1 M $NiSO_4$ was used as the electrolyte. The UPD was achieved by 10 triangular potential scans ranging from -0.15 to 0.45 V vs AgCl/Ag at a scan rate of 20 mV s^{-1}. During the scan, argon was purged continuously. The potentials were controlled with a Gamry Reference 600+ potentiostat.

Electrochemical measurements were carried out in 0.1 M H_2SO_4 in a custom-designed H-type cell separated by a piece of a proton exchange membrane (Nafion® perfluorinated membrane 115). A graphite rod (3 mm, Sigma-Aldrich), instead of platinum was used as the counter electrode to avoid any metallic contamination. All potentials were measured against a Hg_2SO_4/Hg reference electrode (saturated K_2SO_4, BASi®) and converted to the SHE scale using E (vs SHE) = E (vs Hg_2SO_4/Hg) + 0.645 V. Propane was purged continuously at 3 sccm throughout the whole electrolysis.

The gas products were quantified using a gas chromatograph (Agilent 7890B). The gas chromatograph was equipped with a ShinCarbon ST Micropacked GC Column and a 0.5M Hayesep

Q 80/100 UltiMetal packed column. Argon was used as the carrier gas. The liquid products were quantified using a Bruker AVIII 600MHz NMR spectrometer. After electrolysis, 500 μL of the electrolyte was mixed with 100 μL of D_2O (99.9%, Sigma-Aldrich). 50 μM dimethyl sulfoxide (≥99.9%, Alfa Aesar) was added as an internal standard. The mixed solution was pipetted repeatedly to remove dissolved unreacted propane. The ^{1}H spectrum was measured with water suppression using an excitation sculpting method.

ASSOCIATED CONTENT

Supporting Information. This material is available free of charge via the Internet at http://pubs.acs.org.
Supporting data and figures (PDF)

AUTHOR INFORMATION

Corresponding Authors

Qi Lu − State Key Laboratory of Chemical Engineering, Department of Chemical Engineering, Tsinghua University, Beijing 100084, China; orcid.org/0000-0002-0380-2629; Email: luqicheme@mail.tsinghua.edu.cn
Mu-Jeng Cheng − Department of Chemistry, National Cheng Kung University, Tainan 701, Taiwan; orcid.org/0000-0002-8121-0485; Email: mjcheng@mail.ncku.edu.tw
William A. Goddard III − Materials and Process Simulation Center, California Institute of Technology, Pasadena, California 91125, USA; orcid.org/0000-0003-0097-5716; Email: wag@caltech.edu

Authors

Haochen Zhang − State Key Laboratory of Chemical Engineering, Department of Chemical Engineering, Tsinghua University, Beijing 100084, China; orcid.org/0000-0002-2774-5868
Chunsong Li − State Key Laboratory of Chemical Engineering, Department of Chemical Engineering, Tsinghua University, Beijing 100084, China; orcid.org/0000-0002-8016-1896

ACKNOWLEDGMENT

H.Z., C.L. and Q.L. acknowledge the financial support from the National Natural Science Foundation of China (Grant Number 21872079). M.J.C. acknowledge financial support from the Ministry of Science and Technology of the Republic of China under grant no. MOST 109-2113-M-006-009. W.A.G. thanks the US NSF (CBET-2005250) for support. The authors thank Prof. Zhiqiang Niu for advice on underpotential deposition of Ni on Au. All NMR experiments were carried out at BioNMR facility, Tsinghua University Branch of China National Center for Protein Sciences (Beijing). The authors thank Dr. Ning Xu for assistance in NMR data collection. Our calculations were supported by Center of High Performance Computing, Tsinghua University.

REFERENCES

(1) McKean, D. C.; Duncan, J. L.; Batt, L. CH stretching frequencies, bond lengths and dissociation energies. *Spectrochim. Acta A* **1973,** *29*, 1037-1049.
(2) McKean, D. C. Individual CH bond strengths in simple organic compounds: effects of conformation and substitution. *Chem. Soc. Rev.* **1978,** *7*, 399-422.
(3) Blanksby, S. J.; Ellison, G. B. Bond dissociation energies of organic molecules. *Acc. Chem. Res.* **2003,** *36*, 255-263.
(4) You, B.; Liu, X.; Liu, X.; Sun, Y. Efficient H2 Evolution Coupled with Oxidative Refining of Alcohols via A Hierarchically Porous Nickel Bifunctional Electrocatalyst. *ACS Catal.* **2017,** *7*, 4564-4570.
(5) Wei, X.; Wang, S.; Hua, Z.; Chen, L.; Shi, J. Metal-Organic Framework Nanosheet Electrocatalysts for Efficient H2 Production from Methanol Solution: Methanol-Assisted Water Splitting or Methanol Reforming? *ACS Appl. Mater. Interfaces* **2018,** *10*, 25422-25428.
(6) Verma, S.; Lu, S.; Kenis, P. J. A. Co-electrolysis of CO2 and glycerol as a pathway to carbon chemicals with improved technoeconomics due to low electricity consumption. *Nat. Energy* **2019,** *4*, 466-474.
(7) Xu, Y.; Zhang, B. Recent Advances in Electrochemical Hydrogen Production from Water Assisted by Alternative Oxidation Reactions. *ChemElectroChem* **2019,** *6*, 3214-3226.
(8) Yuan, S.; Li, Y.; Peng, J.; Questell‐Santiago, Y. M.; Akkiraju, K.; Giordano, L.; Zheng, D. J.; Bagi, S.; Román‐Leshkov, Y.; Shao‐Horn, Y. Conversion of Methane into Liquid Fuels—Bridging Thermal Catalysis with Electrocatalysis. *Advanced Energy Materials* **2020,** *10*.
(9) Boyd, M. J.; Latimer, A. A.; Dickens, C. F.; Nielander, A. C.; Hahn, C.; Nørskov, J. K.; Higgins, D. C.; Jaramillo, T. F. Electro-Oxidation of Methane on Platinum under Ambient Conditions. *ACS Catal.* **2019,** *9*, 7578-7587.
(10) O'Reilly, M. E.; Kim, R. S.; Oh, S.; Surendranath, Y. Catalytic Methane Monofunctionalization by an Electrogenerated High-Valent Pd Intermediate. *ACS Cent. Sci.* **2017,** *3*, 1174-1179.
(11) Kim, R. S.; Surendranath, Y. Electrochemical Reoxidation Enables Continuous Methane-to-Methanol Catalysis with Aqueous Pt Salts. *ACS Cent. Sci.* **2019,** *5*, 1179-1186.
(12) Deng, J.; Lin, S. C.; Fuller, J., 3rd; Iniguez, J. A.; Xiang, D.; Yang, D.; Chan, G.; Chen, H. M.; Alexandrova, A. N.; Liu, C. Ambient methane functionalization initiated by electrochemical oxidation of a vanadium (V)-oxo dimer. *Nat. Commun.* **2020,** *11*, 3686.
(13) Frese Jr, K. W. Partial electrochemical oxidation of methane under mild conditions. *Langmuir* **1991,** *7*, 13-15.
(14) Yoo, J. S.; Khan, T. S.; Abild-Pedersen, F.; Nørskov, J. K.; Studt, F. On the role of the surface oxygen species during A-H (A = C, N, O) bond activation: a density functional theory study. *Chem. Commun.* **2015,** *51*, 2621-2624.
(15) Hibbitts, D.; Neurock, M. Promotional effects of chemisorbed oxygen and hydroxide in the activation of C–H and O–H bonds over transition metal surfaces. *Surf. Sci.* **2016,** *650*, 210-220.
(16) Varghese, J. J.; Trinh, Q. T.; Mushrif, S. H. Insights into the synergistic role of metal–lattice oxygen site pairs in four-centered C–H bond activation of methane: the case of CuO. *Catal. Sci. Technol.* **2016,** *6*, 3984-3996.
(17) Niu, T.; Jiang, Z.; Zhu, Y.; Zhou, G.; van Spronsen, M. A.; Tenney, S. A.; Boscoboinik, J. A.; Stacchiola, D. Oxygen-Promoted Methane Activation on Copper. *J. Phys. Chem. B* **2018,** *122*, 855-863.
(18) Arnarson, L.; Schmidt, P. S.; Pandey, M.; Bagger, A.; Thygesen, K. S.; Stephens, I. E. L.; Rossmeisl, J. Fundamental limitation of electrocatalytic methane conversion to methanol. *Phys. Chem. Chem. Phys.* **2018,** *20*, 11152-11159.

(19) Latimer, A. A.; Aljama, H.; Kakekhani, A.; Yoo, J. S.; Kulkarni, A.; Tsai, C.; Garcia-Melchor, M.; Abild-Pedersen, F.; Nørskov, J. K. Mechanistic insights into heterogeneous methane activation. *Phys. Chem. Chem. Phys.* **2017,** *19*, 3575-3581.
(20) Otsuka, K.; Yamanaka, I. Electrochemical cells as reactors for selective oxygenation of hydrocarbons at low temperature. *Catal. Today* **1998,** *41*, 311-325.
(21) Yamanaka, I.; Hasegawa, S.; Otsuka, K. Partial oxidation of light alkanes by reductive activated oxygen over the (Pd-black + VO(acac)2/VGCF) cathode of H2–O2 cell system at 298 K. *Appl. Catal., A: Gen.* **2002,** *226*, 305-315.
(22) Tomita, A.; Nakajima, J.; Hibino, T. Direct oxidation of methane to methanol at low temperature and pressure in an electrochemical fuel cell. *Angew. Chem. Int. Ed. Engl.* **2008,** *47*, 1462-1464.
(23) Lee, B.; Sakamoto, Y.; Hirabayashi, D.; Suzuki, K.; Hibino, T. Direct oxidation of methane to methanol over proton conductor/metal mixed catalysts. *J. Catal.* **2010,** *271*, 195-200.
(24) Lee, B.; Hibino, T. Efficient and selective formation of methanol from methane in a fuel cell-type reactor. *J. Catal.* **2011,** *279*, 233-240.
(25) Greeley, J. Theoretical Heterogeneous Catalysis: Scaling Relationships and Computational Catalyst Design. *Annu. Rev. Chem. Biomol. Eng.* **2016,** *7*, 605-635.
(26) Hannagan, R. T.; Giannakakis, G.; Flytzani-Stephanopoulos, M.; Sykes, E. C. H. Single-Atom Alloy Catalysis. *Chem. Rev.* **2020,** *120*, 12044-12088.
(27) Goodpaster, J. D.; Bell, A. T.; Head-Gordon, M. Identification of Possible Pathways for C-C Bond Formation during Electrochemical Reduction of CO2: New Theoretical Insights from an Improved Electrochemical Model. *J. Phys. Chem. Lett.* **2016,** *7*, 1471-1477.
(28) Xiao, H.; Cheng, T.; Goddard, W. A., 3rd; Sundararaman, R. Mechanistic Explanation of the pH Dependence and Onset Potentials for Hydrocarbon Products from Electrochemical Reduction of CO on Cu (111). *J. Am. Chem. Soc.* **2016,** *138*, 483-486.
(29) Xiao, H.; Cheng, T.; Goddard, W. A., 3rd Atomistic Mechanisms Underlying Selectivities in C(1) and C(2) Products from Electrochemical Reduction of CO on Cu(111). *J. Am. Chem. Soc.* **2017,** *139*, 130-136.
(30) Zhang, H.; Goddard, W. A.; Lu, Q.; Cheng, M. J. The importance of grand-canonical quantum mechanical methods to describe the effect of electrode potential on the stability of intermediates involved in both electrochemical CO2 reduction and hydrogen evolution. *Phys. Chem. Chem. Phys.* **2018,** *20*, 2549-2557.
(31) Aich, P.; Wei, H. J.; Basan, B.; Kropf, A. J.; Schweitzer, N. M.; Marshall, C. L.; Miller, J. T.; Meyer, R. Single-Atom Alloy Pd-Ag Catalyst for Selective Hydrogenation of Acrolein. *J. Phys. Chem. C* **2015,** *119*, 18140-18148.
(32) Wang, Z. T.; Darby, M. T.; Therrien, A. J.; El-Soda, M.; Michaelides, A.; Stamatakis, M.; Sykes, E. C. H. Preparation, Structure, and Surface Chemistry of Ni-Au Single Atom Alloys. *J. Phys. Chem. C* **2016,** *120*, 13574-13580.
(33) Lucci, F. R.; Darby, M. T.; Mattera, M. F.; Ivimey, C. J.; Therrien, A. J.; Michaelides, A.; Stamatakis, M.; Sykes, E. C. Controlling Hydrogen Activation, Spillover, and Desorption with Pd-Au Single-Atom Alloys. *J. Phys. Chem. Lett.* **2016,** *7*, 480-485.
(34) Lucci, F. R.; Zhang, L.; Thuening, T.; Uhlman, M. B.; Schilling, A. C.; Henkelman, G.; Charles H. Sykes, E. The effect of single pd atoms on the energetics of recombinative O2 desorption from Au(111). *Surf. Sci.* **2018,** *677*, 296-300.
(35) Zhang, J.; Zhang, H.; Cheng, M. J.; Lu, Q. Tailoring the Electrochemical Production of H2 O2 : Strategies for the Rational Design of High-Performance Electrocatalysts. *Small* **2020,** *16*, e1902845.
(36) Luo, J.-H.; Hong, Z.-S.; Chao, T.-H.; Cheng, M.-J. Quantum Mechanical Screening of Metal-N4-Functionalized Graphenes for Electrochemical Anodic Oxidation of Light Alkanes to Oxygenates. *J. Phys. Chem. C* **2019,** *123*, 19033-19044.
(37) O'Halloran, K. P.; Zhao, C.; Ando, N. S.; Schultz, A. J.; Koetzle, T. F.; Piccoli, P. M.; Hedman, B.; Hodgson, K. O.; Bobyr, E.; Kirk, M. L.; Knottenbelt, S.; Depperman, E. C.; Stein, B.; Anderson, T. M.; Cao, R.; Geletii, Y. V.; Hardcastle, K. I.; Musaev, D. G.; Neiwert, W. A.; Fang, X.; Morokuma, K.; Wu, S.; Kogerler, P.; Hill, C. L. Revisiting the polyoxometalate-based late-transition-metal-oxo complexes: the "oxo wall" stands. *Inorg. Chem.* **2012,** *51*, 7025-7031.
(38) Ray, K.; Heims, F.; Pfaff, F. F. Terminal Oxo and Imido Transition-Metal Complexes of Groups 9-11. *Eur. J. Inorg. Chem.* **2013,** *2013*, 3784-3807.
(39) Kepp, K. P. A Quantitative Scale of Oxophilicity and Thiophilicity. *Inorg. Chem.* **2016,** *55*, 9461-9470.
(40) Moltved, K. A.; Kepp, K. P. The Chemical Bond between Transition Metals and Oxygen: Electronegativity, d-Orbital Effects, and Oxophilicity as Descriptors of Metal-Oxygen Interactions. *J. Phys. Chem. C* **2019,** *123*, 18432-18444.
(41) Chang, K.; Zhang, H. C.; Chen, J. G. G.; Lu, Q.; Cheng, M. J. Constant Electrode Potential Quantum Mechanical Study of CO2 Electrochemical Reduction Catalyzed by N-Doped Graphene. *ACS Catal.* **2019,** *9*, 8197-8207.
(42) Wellendorff, J.; Lundgaard, K. T.; Mogelhoj, A.; Petzold, V.; Landis, D. D.; Nørskov, J. K.; Bligaard, T.; Jacobsen, K. W. Density functionals for surface science: Exchange-correlation model development with Bayesian error estimation. *Phys. Rev. B* **2012,** *85*.
(43) Medford, A. J.; Wellendorff, J.; Vojvodic, A.; Studt, F.; Abild-Pedersen, F.; Jacobsen, K. W.; Bligaard, T.; Nørskov, J. K. Catalysis. Assessing the reliability of calculated catalytic ammonia synthesis rates. *Science* **2014,** *345*, 197-200.
(44) Tsai, C.; Latimer, A. A.; Yoo, J. S.; Studt, F.; Abild-Pedersen, F. Predicting Promoter-Induced Bond Activation on Solid Catalysts Using Elementary Bond Orders. *J. Phys. Chem. Lett.* **2015,** *6*, 3670-3674.
(45) Latimer, A. A.; Kulkarni, A. R.; Aljama, H.; Montoya, J. H.; Yoo, J. S.; Tsai, C.; Abild-Pedersen, F.; Studt, F.; Nørskov, J. K. Understanding trends in C-H bond

activation in heterogeneous catalysis. *Nat. Mater.* **2017,** *16*, 225-229.
(46) Bubendorff, J. L.; Cagnon, L.; CostaKieling, V.; Bucher, J. P.; Allongue, P. Anion promoted Ni-underpotential deposition on Au(111). *Surf. Sci.* **1997,** *384*, L836-L843.
(47) Parida, S.; Kramer, D.; Volkert, C. A.; Rosner, H.; Erlebacher, J.; Weissmuller, J. Volume change during the formation of nanoporous gold by dealloying. *Phys. Rev. Lett.* **2006,** *97*, 035504.
(48) Koh, S.; Strasser, P. Electrocatalysis on bimetallic surfaces: modifying catalytic reactivity for oxygen reduction by voltammetric surface dealloying. *J. Am. Chem. Soc.* **2007,** *129*, 12624-12625.
(49) Snyder, J.; Asanithi, P.; Dalton, A. B.; Erlebacher, J. Stabilized Nanoporous Metals by Dealloying Ternary Alloy Precursors. *Adv. Mater.* **2008,** *20*, 4883-4886.
(50) Strasser, P.; Koh, S.; Anniyev, T.; Greeley, J.; More, K.; Yu, C.; Liu, Z.; Kaya, S.; Nordlund, D.; Ogasawara, H.; Toney, M. F.; Nilsson, A. Lattice-strain control of the activity in dealloyed core-shell fuel cell catalysts. *Nat Chem* **2010,** *2*, 454-460.
(51) Cui, C.; Gan, L.; Li, H. H.; Yu, S. H.; Heggen, M.; Strasser, P. Octahedral PtNi nanoparticle catalysts: exceptional oxygen reduction activity by tuning the alloy particle surface composition. *Nano Lett.* **2012,** *12*, 5885-5889.
(52) Cui, C.; Gan, L.; Heggen, M.; Rudi, S.; Strasser, P. Compositional segregation in shaped Pt alloy nanoparticles and their structural behaviour during electrocatalysis. *Nat. Mater.* **2013,** *12*, 765-771.
(53) Kresse, G.; Hafner, J. Ab initio molecular dynamics for liquid metals. *Phys. Rev. B: Condens. Matter* **1993,** *47*, 558-561.
(54) Kresse, G.; Hafner, J. Ab initio molecular-dynamics simulation of the liquid-metal-amorphous-semiconductor transition in germanium. *Phys. Rev. B: Condens. Matter* **1994,** *49*, 14251-14269.
(55) Kresse, G.; Joubert, D. From ultrasoft pseudopotentials to the projector augmented-wave method. *Phys. Rev. B* **1999,** *59*, 1758-1775.
(56) Hobbs, D.; Kresse, G.; Hafner, J. Fully unconstrained noncollinear magnetism within the projector augmented-wave method. *Phys. Rev. B* **2000,** *62*, 11556-11570.
(57) Perdew, J. P.; Burke, K.; Ernzerhof, M. Generalized gradient approximation made simple. *Phys. Rev. Lett.* **1996,** *77*, 3865-3868.
(58) Grimme, S. Semiempirical GGA-type density functional constructed with a long-range dispersion correction. *J. Comput. Chem.* **2006,** *27*, 1787-1799.
(59) Amft, M.; Lebegue, S.; Eriksson, O.; Skorodumova, N. V. Adsorption of Cu, Ag, and Au atoms on graphene including van der Waals interactions. *J Phys Condens Matter* **2011,** *23*, 395001.
(60) Nørskov, J. K.; Rossmeisl, J.; Logadottir, A.; Lindqvist, L.; Kitchin, J. R.; Bligaard, T.; Jonsson, H. Origin of the overpotential for oxygen reduction at a fuel-cell cathode. *J. Phys. Chem. B* **2004,** *108*, 17886-17892.
(61) Zhang, H.; Chang, X.; Chen, J. G.; Goddard, W. A., 3rd; Xu, B.; Cheng, M. J.; Lu, Q. Computational and experimental demonstrations of one-pot tandem catalysis for electrochemical carbon dioxide reduction to methane. *Nat. Commun.* **2019,** *10*, 3340.
(62) Chang, K.; Chen, J. G.; Lu, Q.; Cheng, M. J. Quantum Mechanical Study of N-Heterocyclic Carbene Adsorption on Au Surfaces. *J. Phys. Chem. A* **2017,** *121*, 2674-2682.
(63) Henkelman, G.; Jonsson, H. Improved tangent estimate in the nudged elastic band method for finding minimum energy paths and saddle points. *J. Chem. Phys.* **2000,** *113*, 9978-9985.
(64) Henkelman, G.; Jonsson, H. A dimer method for finding saddle points on high dimensional potential surfaces using only first derivatives. *J. Chem. Phys.* **1999,** *111*, 7010-7022.

TOC Graphic